Destabilizing high-capacity high entropy hydrides via earth abundant substitutions: From predictions to experimental validation

Andrei Agafonov, Nayely Pineda-Romero, Matthew Witman, V. Nassif, Gavin B.M. Vaughan, Lei Lei, Sanliang Ling, David M Grant, Martin Dornheim, Mark Allendorf, et al.

To cite this version:

Andrei Agafonov, Nayely Pineda-Romero, Matthew Witman, V. Nassif, Gavin B.M. Vaughan, et al.. Destabilizing high-capacity high entropy hydrides via earth abundant substitutions: From predictions to experimental validation. Acta Materialia, 2024, 276, pp.120086. 10.1016/j.actamat.2024.120086 . hal-04670840

HAL Id: hal-04670840
https://hal.science/hal-04670840v1

Submitted on 13 Aug 2024

Destabilizing high-capacity high entropy hydrides via earth abundant substitutions: from predictions to experimental validation

Andrei Agafonov[1], Nayely Pineda-Romero[1], Matthew Witman[2*], Vivian Nassif [3], Gavin B. M. Vaughan[4], Lei Lei[5], Sanliang Ling[5*], David M. Grant[5], Martin Dornheim[5], Mark Allendorf[2], Vitalie Stavila[2] and Claudia Zlotea[1*]

[1] Univ. Paris-Est Creteil, CNRS, ICMPE, UMR 7182, 2 Rue Henri Dunant, 94320, Thiais, France

[2] Sandia National Laboratories, Livermore, California 94551, United States

[3] CNRS, Université Grenoble Alpes, Institut Néel, 38042 Grenoble, France

[4] ESRF-The European Synchrotron, 71, Avenue des Martyrs, CEDEX 9, 38042 Grenoble, France

[5] Advanced Materials Research Group, Faculty of Engineering, University of Nottingham, Nottingham NG7 2RD, U.K.

*Corresponding authors emails: claudia.zlotea@cnrs.fr; mwitman@sandia.gov; sanliang.Ling@nottingham.ac.uk

Abstract

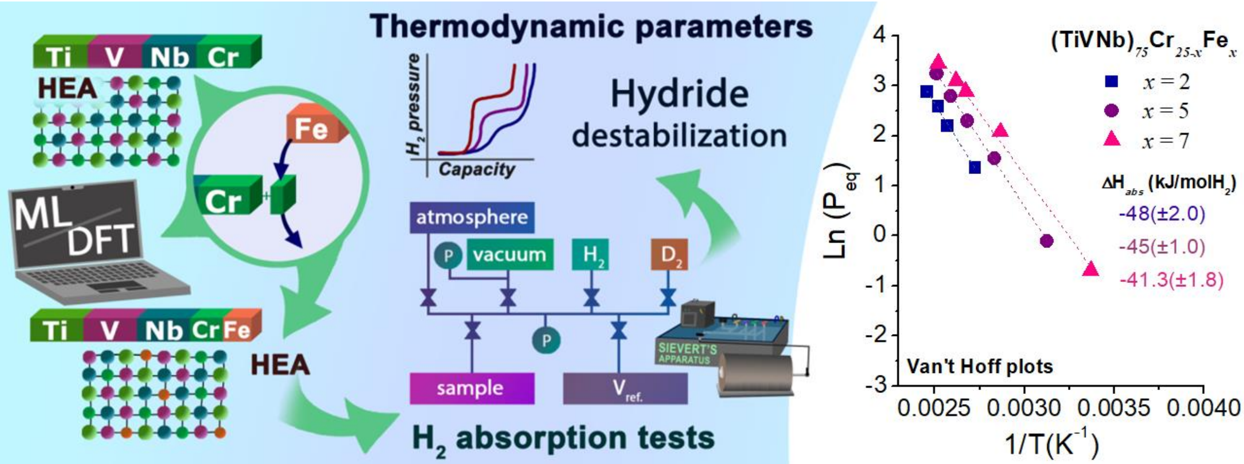

Abstract

The vast chemical space of high entropy alloys (HEAs) makes trial-and-error experimental approaches for materials discovery intractable and often necessitates data-driven and/or first principles computational insights to successfully target materials with desired properties. In the context of materials discovery for hydrogen storage applications, a theoretical prediction-experimental validation approach can vastly accelerate the search for substitution strategies to destabilize high-capacity hydrides based on benchmark HEAs, e.g. TiVNbCr alloys. Here, machine learning predictions, corroborated by DFT calculations, predict substantial hydride destabilization with increasing substitution of earth-abundant Fe content in the $(TiVNb)_{75}Cr_{25-x}Fe_x$ system. The as-prepared alloys crystallize in a single-phase *bcc* lattice for limited Fe content $x < 7$, while larger Fe content favors the formation of a secondary C14 Laves phase intermetallic. Short range order for alloys with $x < 7$ can be well described by a random distribution of atoms within the *bcc* lattice without lattice distortion. Hydrogen absorption experiments performed on selected alloys validate the predicted thermodynamic destabilization of the corresponding *fcc* hydrides and demonstrate promising lifecycle performance through reversible absorption/desorption. This demonstrates the potential of computationally expedited hydride discovery and points to further opportunities for optimizing *bcc* alloy ↔ *fcc* hydrides for practical hydrogen storage applications.

Key words: high entropy alloys, hydrogen storage, machine learning, density functional theory, neutron diffraction, synchrotron X-ray diffraction, pair distribution function

Introduction

Hydrogen shows great potential as a clean energy carrier that can be produced, stored, and utilized at scale without harmful emissions. However, a primary obstacle to the widespread adoption of hydrogen technologies is safe, compact, efficient, and low-cost storage [1]. Among the various H_2 storage strategies, solid-state H_2 storage in the form of high-capacity metal hydrides is one of the most compelling alternatives to compressed gas to improve the safety, efficiency, and compactness of practical energy storage systems [2]. Substantial research efforts for many years have been aimed at finding new materials capable of achieving high reversible capacity under near-ambient conditions, however many challenges persist, notably concerning cost and roundtrip energy-efficiency [1].

Hydrides of many metals and conventional alloys/intermetallics exhibit high reversibility and volumetric H_2 storage density values surpassing those of compressed hydrogen gas, but often suffer from thermodynamic and/or kinetic limitations [3]. The relatively new class of high-entropy alloys (HEAs), solid solutions with at least 5 elements with atomic concentrations from 5 to 35%, are particularly interesting for H_2 storage [4,5]. Among several types of lattices adopted by HEA solid solutions (*bcc*, *fcc*, *hcp*), *bcc* alloys that undergo a phase transition to *fcc* dihydrides demonstrate exceptionally high hydrogen per metal (H/M) capacities and good reversibility. Yet, these advantages are frequently offset by unfavorably high stability of the *fcc* hydride, resulting in elevated desorption temperatures [6,7]. Many theoretical and experimental efforts are currently devoted to control the thermodynamics of the hydride formation to provide an optimum destabilization, which is necessary to ensure the material reversibility close to ambient conditions [8]. Compositional machine learning (ML) models for hydride thermodynamics have proven useful for approximate but computationally cheap and experimentally verifiable predictions of substitution strategies to destabilize hydrides of (high entropy) alloys [9,10].

Among numerous *bcc* HEA alloys that form *fcc* hydrides, those based on TiVNb have demonstrated extremely high saturation capacities around 2 H/M but at the cost of unfavorable desorption enthalpies ($\Delta H \sim 50 - 70$ kJ/mol H_2) [11,12]. Adding elements with low hydrogen affinity, e.g., (TiVNb)X where $X = \{\mathrm{Cr, Al, Mo}\}$ has been demonstrated to significantly destabilize the *fcc* hydride phase and reduce the desorption enthalpies to as low as ~40 kJ/mol H_2 [13–15]. Nonetheless, due to the substantial chemical tunability of HEAs, there is a need for continued investigation of novel X that can yield Pareto optimal hydrogen storage materials [16], i.e., hydrides that optimally balance the competing tradeoffs between high capacity, low ΔH, and low raw material costs.

Here, we consider the substitution of elements in X (specifically Cr) with Fe, which we hypothesize, can further destabilize the hydride phase. To our knowledge there are no reports in the literature focused on this strategy. We describe machine learning (ML) predictions and density functional theory (DFT) calculations that support this hypothesis and indicate that the equilibrium plateau pressure could be varied in a wide range by relatively small changes in composition. Beyond any potential technical improvement in hydrogen storage properties, proposing Fe substitution also has cost benefits since (1) it is cheap and earth abundant and (2) niobium and vanadium, the higher-cost elements in this composition, are often extracted from naturally occurring ferrovanadium and ferroniobium. These pre-alloys are substantially cheaper than pure vanadium and niobium and could potentially be used as the synthetic precursors to reduce material cost [17]. After predicting thermodynamic destabilization of hydrides in the series $(\mathrm{TiVNb})_{75}\mathrm{Cr}_{25-x}\mathrm{Fe}_x$, we then performed a detailed experimental characterization of the alloys with $x = 2$-15 as well as the equimolar TiVCrFeNb. Selected compositions are extensively studied by *ex situ* and *in situ* neutron diffraction (ND), *ex situ* synchrotron X-ray diffraction (SR-XRD) with related pair distribution function (PDF) analysis, thermo-desorption spectroscopy (TDS) and absorption/desorption cycling. This provides a holistic picture of the hydride destabilization upon iron addition, including the improved performance under repeated cycling, and highlights opportunities for further optimization of this system for improved hydrogen storage performance.

Materials and methods

Computational methods. Details on the machine learning methodology, model cross-validation, and DFT calculations are provided in the Supplementary Information (SI) shown in Section SI1 and SI2, respectively.

Alloy synthesis. High purity metals were used as feedstock material: Ti (NEYCO titanium 99.99% pellets), V (NEYCO vanadium 99.9% pellets), Nb (NEYCO niobium 99.95% pellets), Cr (ChemPur chromium 99.99% pieces), Fe (Alfa Aesar iron 99.97% pieces).

The $(TiVNb)_{75}Cr_{25-x}Fe_x$ (x = 2-15) alloys and equimolar TiVNbCrFe composition were prepared by arc-melting in an electric arc furnace under Ar atmosphere (≈ 300 mbar) and recast 10 times by flipping the ingot between each melting to achieve good homogeneity. The total mass of each alloy sample was 3±0.0005 g.

Powder X-ray diffraction. The sample crystalline structures (alloys and hydrides) were investigated by powder X-ray diffraction (XRD) using a D8 Advance Bruker diffractometer (Cu-K_α radiation $\lambda = 1.5406$ Å, Bragg-Brentano Geometry) in the 2θ range 30 - 90°. The XRD patterns were refined using the fundamental parameters approach implemented in TOPAS Bruker software to estimate the lattice parameters and phase fractions.

Synchrotron X-ray diffraction. High-energy synchrotron X-ray diffraction (SR-XRD) measurements were carried out at the ID15A beamline at ESRF, Grenoble (France) [18]. Powder samples were placed in a borosilicate capillary and the energy of the incident beam was 98 keV ($\lambda = 0.1265$ Å). Two dimensional XRD patterns were obtained from a Pilatus 2M CdTe detector, and azimuthally integrated with locally modified version of pyFAI with corrections applied for detector response [19]. G(r) profiles were obtained from the integrated patterns using pdfgetx3 [20]. The structural analysis was carried out using the PDFgui free software [21]. The SR-XRD patterns were refined using the Rietveld method as implemented in the FullProf free software [22].

Hydrogen absorption measurements. The hydrogenation process was carried out on selected alloys with $x = 2$, 5 and 7 using a Sievert apparatus, which consisted of a home-made manual manometric device with thermostatically calibrated volumes. The stainless-steel sample holder was filled with about 400 mg of the alloy, sealed using a metal gasket to prevent gas leakage and connected to the Sievert apparatus. Before starting the hydrogenation process, an activation procedure was carried out at 410 °C under dynamic secondary vacuum (10^{-3} mbar) for 24 hours. Two types of measurements were carried out: (1) absorption kinetics and cycling tests at 25 °C and (2) absorption PCIs for a range of temperatures for selected alloys with $x = 2$, 5 and 7. For the absorption kinetics, the sample holder was placed in a water bath under isothermal conditions (25 °C) and high H_2 pressure (~ 37 bar). For acquisition of the PCIs, small H_2 doses were used up to 65 bar. A furnace was used for the acquisition of PCIs at temperatures higher than 25 °C. The mass of the samples was measured before hydrogenation to calculate the samples volume values and then the values of the storage capacity using the real gas state equation for H_2 from GASPAK Version 3.32 (Horizon Technologies). The cycling tests were carried out under a final 35 bar H_2 pressure at 25 °C until reaching equilibrium and dynamic vacuum at 410 °C for 3 hours for absorption and desorption, respectively.

Neutron diffraction studies. Deuteration was used in the framework of the sample's preparation for this analysis. The procedure was similar as for H_2 absorption kinetics and the final pressure was around 14±5 bar of D_2. Selected deuterated $(TiVNb)_{75}Cr_{25-x}Fe_x$ ($x = 2$, 5 and 7) alloys were characterized by *ex situ* powder neutron diffraction on the D1B beamline at the Institute Laue-Langevin, Grenoble, France ($\lambda = 1.2858$ Å) with a scanning range of 2θ from 1 to 128°, using a vanadium container (DOI:10.5291/ILL-DATA.5-25-284). The neutron powder diffraction data was refined using the Rietveld method with FullProf software [22], where the peak shape was described by Thompson-Cox-Hastings Pseudo Voigt function. The deuterated sample with $x = 5$ was also characterized by the *in situ* powder neutron diffraction during deuterium thermo-desorption. The measurements were performed in a silica tube containing the deuterated powder sample, connected to a secondary vacuum and with a constant heating rate of 1 °C/min while the evolved gas pressure was recorded with a vacuum gauge. The lattice parameters thermal evolution was determined by Le Bail fitting [23] implemented in FullProf software.

Scanning electron microscopy. The microstructure was analyzed by scanning electron microscopy (SEM) using a Zeiss Merlin instrument equipped with an EDS (energy-dispersive X-ray spectroscopy) detector. The powder samples were placed in an epoxy resin, polished with various abrasive sizes (finally with 3 microns) and coated with a 1.5–2.5 nm Pd layer directly before the SEM analysis. For elemental analysis, an accelerated electron voltage of 15 keV was used and the element quantification was performed using Ti($K_{\alpha 1}$), V($K_{\alpha 1}$), Nb($L_{\alpha 1}$), Cr($K_{\alpha 1}$) and Fe($K_{\alpha 1}$) signals. The analyses were carried out for the as-synthesized, hydrogenated alloys and the alloy materials after cycling tests.

Thermal desorption spectroscopy. The hydrogen desorption properties for the hydrogenated alloys were analyzed by a home-made thermal desorption spectroscopy (TDS) using a quadrupole mass spectrometer (QMS) [24]. About 10 mg of the hydride sample was loaded into the sample holder each time and then connected to the QMS, working under secondary vacuum (1×10^{-6} mbar). The desorption profile (partial pressures of released gases) was recorded by heating the sample at a constant rate of 5 °C/min up to 450 °C.

Results and discussion

Compositional ML model predictions of Fe destabilization

We updated the ML-ready HydPARK database to v0.0.6 [25] with recent literature data for (TiVNb)X [5,15,26,27], retrained/validated gradient boosting tree models for hydride thermodynamics [9,10] (see Supplementary Section 1, Figure SI1 for details) using Magpie [28] and custom features derived from the alloy composition, and finally predict hydride thermodynamic properties of the Fe-substituted series $(TiVNb)_{75}Cr_{25-x}Fe_x$ ($0 < x < 20$). Increasing x is predicted by the compositional ML model to further destabilize the hydride phase by decreasing ΔH (Figure 1a), commensurate with a predicted drop in the saturation capacity (Figure 1b). Note that $x = 0$ is a composition represented in the v0.0.6 database with $\Delta H = 48$ kJ/molH$_2$ extracted from Ref. [26]. Figure 1c plots the global summary of the ΔH model's Shapely Additive Prediction (SHAP) values [29], i.e., the impact on the model's output (x-axis) attributed the value (color code) to each feature (row) for a given prediction (scatter point). Here only the top 5 most important features (rows), as quantified by the sum of absolute SHAP values for a given feature, are visualized and correspond to composition-weighted averages of an elemental property, $\bar{p} = \sum_i x_i p_i$ ($x_i \equiv$ atomic fraction of element i, $p_i \equiv$ the elemental property). These properties include Magpie features ($r_c \equiv$ covalent radius, Me# $\equiv$ Mendeleev number, $T_m \equiv$ melting temperature, $\chi \equiv$ Pauling electronegativity) and a hydride specific feature ($\Delta H_b \equiv$ binary hydride formation enthalpy from the Materials Project). Large variation in SHAP values (impact on predicted ΔH) is only observed for $\bar{\chi}$, i.e., the model mainly utilizes the increased average electronegativity with Fe substitution for Cr to explain the decrease in ΔH.

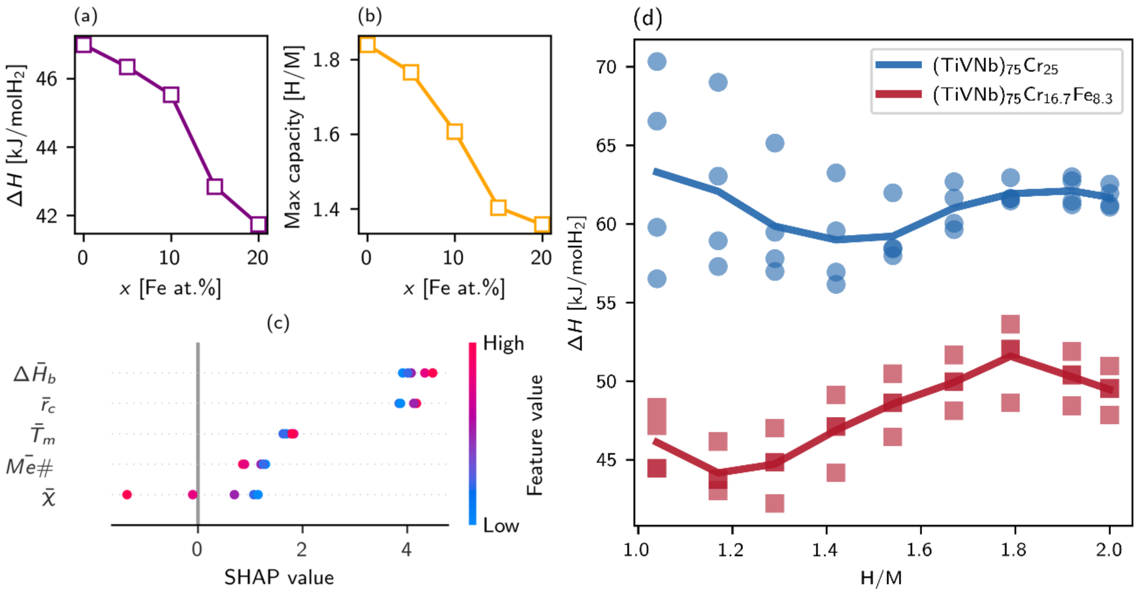

Figure 1. ML-predicted (a) desorption enthalpy and (b) max saturation capacity as a function of Fe-substitution, as well as (c) SHAP values for the desorption enthalpy model. (d) Dehydrogenation enthalpy of $(TiVNb)_{75}Cr_{25}$ and $(TiVNb)_{75}Cr_{16.7}Fe_{8.3}$ obtained by DFT calculations. Four *fcc* alloy configurations (one with the lowest, two with medium and one with high formation energy from 100 sampled configurations) are selected for hydride formation, and their dehydrogenation enthalpy at different H/M (between 1.0 and 2.0) were plotted as scatter points. The solid lines are the average dehydrogenation enthalpy of the four selected configurations.

Although methods have been proposed that may address some of its shortcoming [30], this compositional ML model's features are structure agnostic and provide limited predicted information beyond scalar hydride thermodynamic properties. Therefore, density functional theory (DFT) calculations were also performed to confirm ML-predicted destabilization and gain further atomistic understanding of the underlying hydrogen absorption/desorption mechanism.

Density functional theory calculations of Fe destabilization

To corroborate the ML predictions, we probed the hydride dehydrogenation enthalpy with density functional theory (DFT) calculations (Supplementary Section 2, Figure SI2-1 and Figure SI2-2 for details). Random configurations of the same chemical composition but differing metal distributions on the *fcc* lattice were generated for $(TiVNb)_{75}Cr_{25}$ and $(TiVNb)_{75}Cr_{16.7}Fe_{8.3}$. For each composition, four alloy configurations out of 100 are selected for hydrogenation: the one with the lowest formation energy, two with formation energies near the median value, and the other with high formation energy. Hydride structures at varying H/M ratios were generated using a minimum possible H–H distance d_{min} = 1.6 Å chosen to be less than the Switendick criteria [31] while greater than experimentally measured exceptions to this rule [32] as follows. All tetrahedral interstitial sites are identified and sorted ascendingly by the mean electronegativity of the atoms at the vertices. Hydrogen atoms are sequentially placed at these sites except when there is an existing hydrogen atom within d_{min}, in which case the site is skipped. After all tetrahedral sites are exhausted, the same procedure is repeated for octahedral holes (hydrogen atoms are placed if the H–H distance did not fall below d_{min}). The hydrides were then relaxed, and the total energy of the hydrides, $E_{Hydride}$, of the original alloy, E_{HEA}, and of the gas-phase H_2 molecule, E_{H2}, can be used to calculate the dehydrogenation enthalpy at 0 K for a structure with N hydrogen atoms:

$$\Delta H = E_{\mathrm{H}_2} + \frac{2}{N} E_{\mathrm{HEA}} - \frac{2}{N} E_{\mathrm{Hydride}} \qquad \text{(equation 1)}$$

As shown in Figure 1d, within the H/M range of 1.0-2.0, the average dehydrogenation enthalpy of $(TiVNb)_{75}Cr_{16.7}Fe_{8.3}$ is 10-20 kJ/molH_2 lower than that of $(TiVNb)_{75}Cr_{25}$, i.e., substitution of Cr by small amounts of Fe in TiVNbCr substantially destabilizes the hydride phase. Notably, the average dehydrogenation enthalpy in TiVNbCr remains approximately constant in the $1.8 < H/M < 2.0$ range, while it begins to decrease for $H/M > 1.8$ in $(TiVNb)_{75}Cr_{16.7}Fe_{8.3}$, a qualitative hint that the capacity of the latter may be reduced (as later confirmed experimentally). Therefore, the agreement of DFT-calculated reduction in the dehydrogenation enthalpy through Fe substitution of Cr both validated our ML model while providing more detailed atomistic insights on the interaction between hydrogen and different alloy compositions. Note that even closer quantitative agreement in the enthalpy predictions may be achieved in the future with a more rigorous sampling procedures (i.e., Monte Carlo simulations) and by considering correction factors for errors in DFT predictions of hydrogen-metal interactions [33], and also by including zero-point energy contributions.

HEAs synthesis and characterization

Following computational predictions of thermodynamic destabilization by Cr substitution with Fe in TiVNbCr, systematic experimental validation was performed for $(TiVNb)_{75}Cr_{25-x}Fe_x$ with x = 2-15, and the equimolar TiVCrFeNb alloy. Composition-derived parameters previously shown to correlate HEAs with their solid solution formation ability, δ (mean square deviation of atomic size) and VEC (valence electron concentration), are shown in Table 1. An empirical guideline for solid solution formation (δ < 6.6%) [34] is satisfied for $x \leq 15$, although it increases with x and exceeds the empirical threshold for the equimolar composition, suggesting the formation of multiphase alloys with intermetallic precipitates.

Fe content (at. %)	**δ (%)**	**VEC**	**Initial phase**	a_{bcc} **(Å)**	**Hydride phase**	a_{fcc} **(Å)**	**Capacity at 25°C (H/M)**	ΔH_{abs} **(kJ/molH$_2$)**	ΔS_{abs} **(J/K·molH$_2$)**	**Ref.**
0	6.11	5.00	*bcc*	3.132	*fcc*	4.378	2.0	-51.6	-129.3	[14,26]
2	6.283	5.04	*bcc*	3.129(1)	*fcc*	4.371(1)	1.94	-48.0(2.0)	-142(5.2)	present
3	6.290	5.06	*bcc*	3.128(1)	-	-	-	-	-	present
4	6.298	5.08	*bcc*	3.124(1)	-	-	-	-	-	present
5	6.305	5.10	*bcc*	3.123(1)	*fcc*	4.369(1)	1.93	-45(1.0)	-140(1.7)	present
7	6.319	5.14	***bcc*** + *C14*	3.127(1)	***fcc*** + *C14*	4.364(4)	1.79	-41.3(1.8)	134(5.3)	present
8	6.327	5.16	***bcc*** + *C14*	3.123(1)	-	-	-	-	-	present
10	6.341	5.20	***bcc*** + *C14*	3.127(1)	-	-	-	-	-	present
15	6.377	5.30	***bcc*** + *C14*	-	-	-	-	-	-	present
TiVNbCrFe	6.7	5.60	***C14*** + *bcc*	-	***C14*** + *bcc*	-	0.81	-	-	present

Table 1. Empirical physicochemical parameters (δ and VEC) of the as-synthesized $(TiVNb)_{75}Cr_{25-x}Fe_x$ alloys with x = 0-15 and the equimolar TiVCrFeNb composition; the main phase is in bold. Storage capacity and thermodynamic data for selected hydrides.

X-ray diffraction (XRD) patterns shown in Figure 2a demonstrate single-phase *bcc* (space group $Im\bar{3}m$) alloys for $x \leq 5$, while traces of a secondary C14 Laves phase are already evident for $x = 7$ and account for 30% of the phase fraction for $x = 15$. Therefore, the limit of Fe solubility in the quaternary TiVNbCr alloy is in the range 5 – 7 at. %, after which further Fe addition precipitates the formation of a secondary intermetallic phase (despite obeying to the empirical rule $\delta < 6.6\%$).

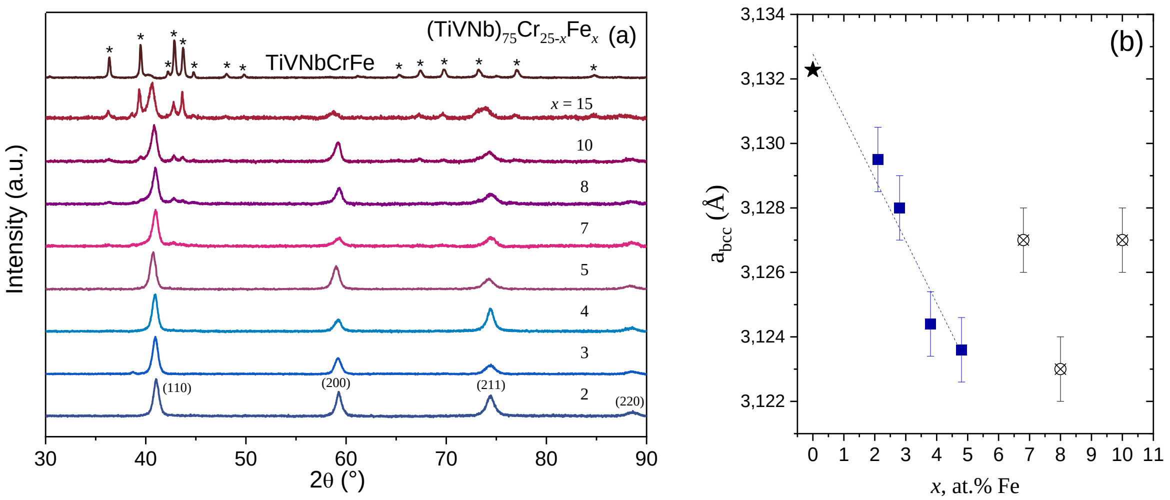

Figure 2. (a) XRD patterns of the as-synthesized $(TiVNb)_{75}Cr_{25-x}Fe_x$ alloys with $x = 2$-15 and the equimolar composition TiVNbCrFe; the diffraction peaks of the C14 hexagonal phase are marked with asterisks and (b) Lattice parameter abcc as a function of Fe content up to $x = 10$; the value for $x = 0$ (star) is taken from reference [26]; the values for single-phase alloys are marked as squares whereas the multi-phased materials are represented as circles with a X; the linear fit for single-phase alloys is a guide for the eyes.

The lattice parameter of the *bcc* phase linearly decreases with increasing Fe concentration (Figure 2b) up to $x = 5$ (for single-phase alloys) due to its smaller atomic radius compared to the other elements ($r_{Ti} = 145$ pm, $r_V = 131$ pm, $r_{Nb} = 143$ pm, $r_{Cr} = 125$ pm, $r_{Fe} = 124$ pm [35]). This correlation breaks down for $x \geq 7$ and is likely associated with the formation of Fe-containing C14 Laves phase that limits the Fe incorporation in the *bcc* lattice. The equimolar TiVNbCrFe sample consists of a dominant C14 Laves intermetallic with a secondary *bcc* phase. Formation of C14 Laves phase has been previously related in closely related compositions [36,37].

The CALPHAD (Calculation of phase diagrams) approach was used to obtain further insights into phase stability in this system (Figure SI3-1). A direct quantitative comparison between these experimental results and CALPHAD predictions is difficult since the as-prepared alloys undergo a rapid quenching from the melt favoring the formation of metastable phases whereas CALPHAD method predicts phases which are in thermodynamic equilibrium. Nevertheless, the formation of *bcc* phase as well as the C14 Laves intermetallics, with the overall composition $(Nb_{23}Ti_{11})(Cr_{36}Fe_{28})$, are predicted via CALPHAD in qualitative agreement with the experiments.

Three $(TiVNb)_{75}Cr_{25-x}Fe_x$ alloys with $x = 2$, 5 and 7 were selected for an in-depth study of the local structure from the pair distribution function (PDF) analysis of synchrotron X-ray total scattering (Figure 3). All PDF profiles are similar, and these alloys have long-range structural correlations. An enlarged zone from 2 to 6 Å is also shown to better appreciate the short-range ordering in these alloys. The alloy with $x = 7$ shows a first intense peak at ~2.7 Å that might contain contributions from both *bcc* and C14 phases and an additional small peak at around 4 Å, most probably from the C14 Laves intermetallic phase. The PDF data fitting is based on an undistorted random *bcc* lattice and shows a good agreement between experimental and calculated profiles, mainly for alloys with $x = 2$ and 5 (Figure SI3-2). This demonstrates that a random distribution of atoms within an undistorted *bcc* lattice, irrespective of the composition, can well describe the atomic arrangement in the low- and high-R regions without any evidence of lattice distortion or preferential ordering or clustering of atoms [5].

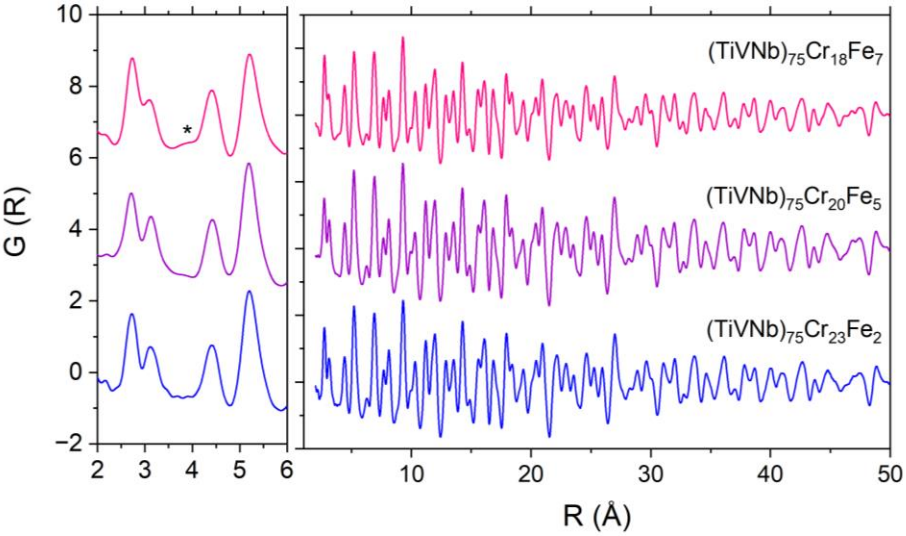

Figure 3. The PDF profiles of the $(TiVNb)_{75}Cr_{25-x}Fe_x$ alloys with $x = 2$, 5 and 7 from total X-ray scattering. An enlarged zone from 2 to 6 Å is also shown in the left-hand side. An additional small peak at around 4 Å marked with an asterisk is present in the alloy with $x = 7$.

The microstructure and chemical homogeneity of all as-synthesized alloys were investigated by SEM-EDS (Figure SI3-3). The average chemical composition agrees well with the nominal values, irrespective of composition (Table SI3-1). Typical for refractory HEAs, dendritic/interdendritic microstructures are observed for the single-phase *bcc* samples which can be attributed to the large difference between the melting temperatures of containing metals and the element partitioning during solidification [38]. The other samples also show dendritic/interdendritic microstructures with Fe rich inclusions from the secondary Laves phase.

Thermodynamics of high entropy hydride formation

Hydrogen sorption properties were investigated for selected alloys with $x = 2$, 5 and 7. The equimolar composition TiVNbCrFe absorbs 0.8 H/M under 60 bar H_2 and 25 °C forming a solid solution with hydrogen (Figure SI3-4) and will not be further considered. The selected alloys with $x = 2$, 5 and 7 quickly absorb hydrogen at room temperature with a high storage capacity (Table 1) around 2 H/M, in agreement with previous results for *bcc* HEAs [4]. The H_2 capacity decreases with the increase in Fe content from 2.0 H/M for TiVNbCr [26] to 1.79 H/M for the alloy with x = 7, in qualitative agreement with ML predictions and DFT calculations (Figure 1). The reduced capacity with increasing Fe content might be reasonably explained by the rigid band model: the addition of a late 3*d* element (second half of 3*d* row) fills the unoccupied valance states of the alloy and consequently decreases the available vacant electronic states for a possible donation of the hydrogen's electron. This reduces the hydrogen storage uptake, as proposed for conventional *bcc* and high entropy materials [39,40].

The absorption PCI curves and related van't Hoff plots for the $(TiVNb)_{75}Cr_{25-x}Fe_x$ alloys with x = 2, 5 and 7 are shown in Figure 4 and the derived thermodynamic properties (ΔH_{abs} and ΔS_{abs}) are listed in Table 1. These alloys undergo a two-step reaction with hydrogen typical for hydrides based on *bcc* alloys and HEAs [5,26,40]: the initial *bcc* alloy absorbs hydrogen forming an intermediate *bcc* monohydride (around 1 H/M) at very low pressure (within the error bar of zero on the pressure transducer ±0.06 bar) and a *fcc* dihydride phase (around 2 H/M) at measurable high pressure. The PCI curves for the second transition occurs at higher pressure at the same temperature (i.e., the *fcc* dihydride is destabilized) and the plateau becomes more sloped with increasing Fe content.

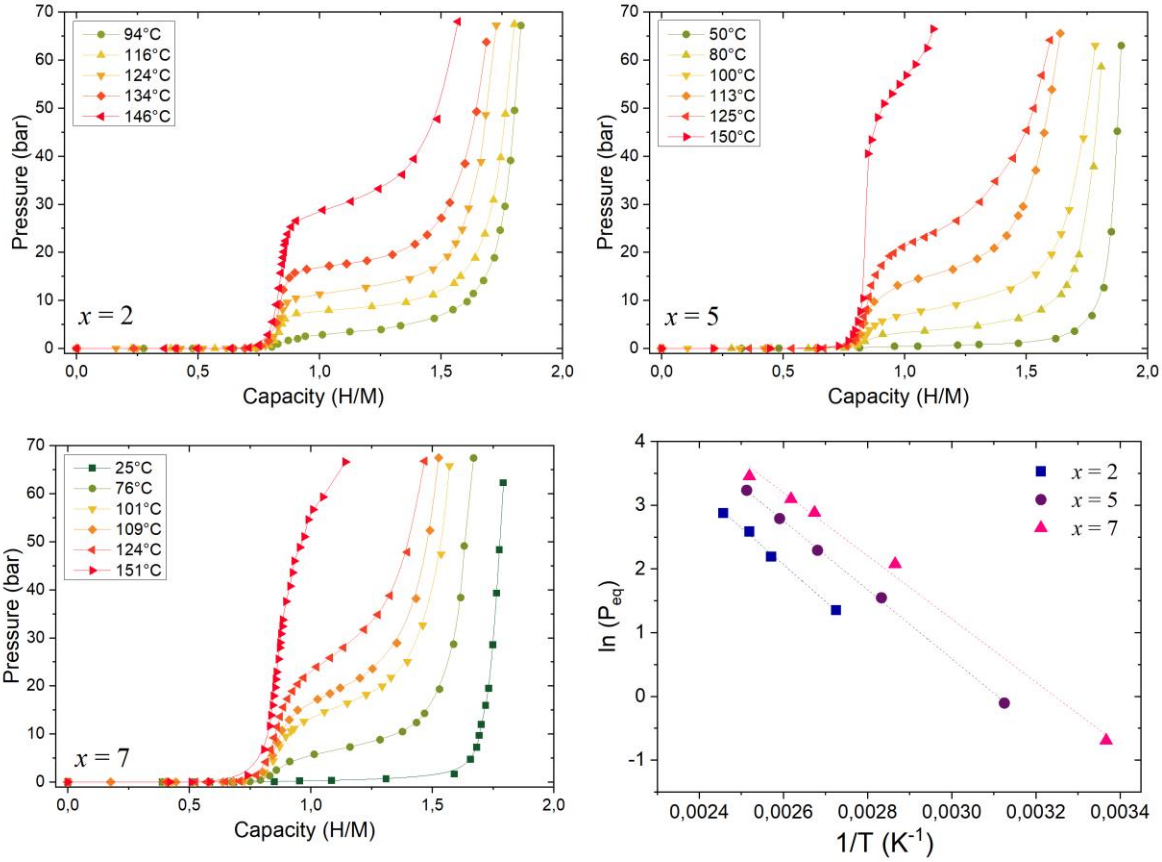

Figure 4. The absorption PCI curves at several temperatures and van't Hoff plots for the $(TiVNb)_{75}Cr_{25-x}Fe_x$ alloys with $x = 2$, 5 and 7.

The TiVNbCr alloy has an enthalpy of absorption ΔH_{abs} = -51.6 kJ/mol H_2 [26], whereas the absolute values obtained for $(TiVNb)_{75}Cr_{25-x}Fe_x$ (x = 2, 5 and 7) decrease with increasing Fe content (Table 1), demonstrating that the presence of Fe destabilizes the hydride phase. This can be rationalized by both steric and electronic effects: i) substitution of Cr with Fe decreases the lattice volume and consequently the available volume of the interstitial sites and therefore the pressure needed to form the hydride increases and ii) the electronegativity of Fe (1.83 on Pauling scale) is higher in comparison with that of Cr (1.66 on Pauling scale) which indicates that the interaction of hydrogen (2.1 on Pauling scale) with tetrahedrons featuring Fe is expected to be less ionic than the interaction of hydrogen with similar tetrahedrons composed of only Cr. These results, in agreement with the ML predictions and DFT calculations, further validate the use of such computational techniques to target hydride destabilization strategies in the complex and vast chemical space of HEA-based hydrides.

Hydride characterization, reversibility, and cycle-life properties

To further assess the hydrogen storage performance of the single-phase alloys, we characterized the crystalline properties of the hydride phases, the phase transition during hydrogen desorption, and the cycle-life stability. Powder XRD diagrams of $(TiVNb)_{75}Cr_{25-x}Fe_x$ (x = 2, 5 and 7) hydrides (lattice parameters are listed in Table 1) and powder neutron diffraction (ND) patterns for the corresponding deuterides are plotted in Figure 5. X-ray and neutron diffraction are complementary techniques, and they explore the metal and hydrogen/deuterium networks of the lattice (the coherent scattering length of the metallic subnetwork is small, around +2 fm, as compared to the corresponding deuteride +15 fm), respectively [41].

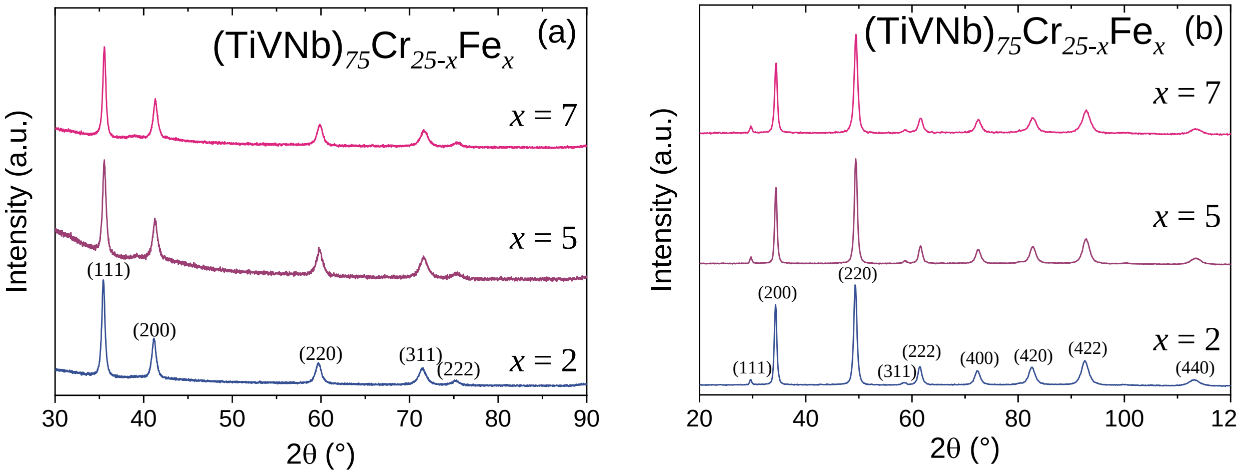

Figure 5. (a) XRD (λ = 1.5406 Å) (b) neutron diffraction (λ = 1.28 Å) diagrams of the hydride/deuteride phases of $(TiVNb)_{75}Cr_{25-x}Fe_x$ with x = 2, 5 and 7.

Both hydrides and deuterides of $(TiVNb)_{75}Cr_{25-x}Fe_x$ alloys with x = 2, 5 and 7 adopt an *fcc* lattice (space group $Fm\bar{3}m$) with hydrogen/deuterium occupying the tetrahedral sites, as previously reported for *bcc* HEAs [4,5]. The lattice parameter decreases as function of Fe content (Table 1), consistent with the lattice parameter of the initial *bcc* alloys (Figure 2b). Interestingly, both X-ray and neutron diffraction patterns of the hydride/deuteride material for $x = 7$ (top of Figure 5), which initially contains about 8 % of C14 intermetallic, show negligeable presence of the secondary phase. This might be reasonably explained by either the overlapping diffraction peaks in the X-ray pattern or the negligible neutron scattering length of the intermetallic Laves phase in the case of neutron diffraction data.

To investigate the reversibility of hydrogen reaction, the desorption process was studied by *in situ* neutron thermo-diffraction for one composition ($x = 5$) and TDS for the hydrides with $x = 2$, 5 and 7. The neutron diffraction patterns during thermal desorption of deuterium (55-425 °C), together with the gas desorption profile and *fcc* lattice parameter variation for the $(TiVNb)_{75}Cr_{20}Fe_5$, are plotted in Figure 6.

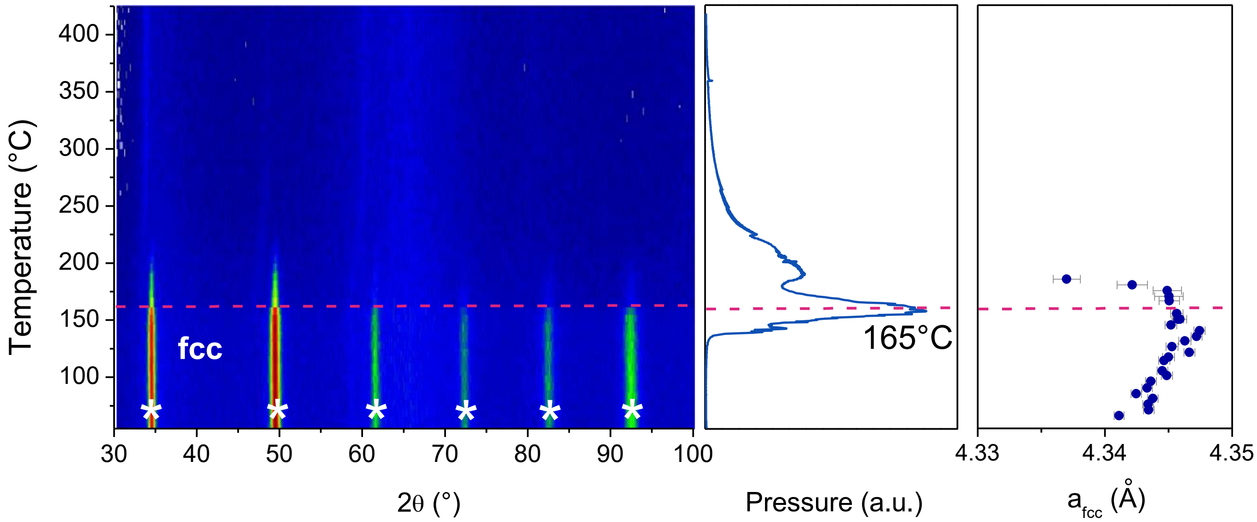

Figure 6. Left-hand panel: in situ neutron diffraction diagrams (λ = 1.28 Å) recorded during thermal desorption from $(TiVNb)_{75}Cr_{20}Fe_5$ deuteride with 1 °C/min (55-425 °C); middle panel: gas desorption profile during desorption; right-hand panel: thermal evolution of the *fcc* lattice parameter.

The initial *fcc* deuteride phase for $x = 5$ is stable up to around 140 °C, during which the lattice parameter steadily increases with temperature. Above this temperature, a main desorption event is observed in the gas profile at 165 °C, followed by a decrease in both the *fcc* peak intensity and the lattice parameter. The diffraction peaks of the desorbed phase are too weak to be accurately measured due to the low mean neutron cross-section of the elements in the alloy composition, a feature already encountered in refractory HEAs [42,43]. The main desorption event at 165 °C marks the loss of ordering of the deuterium network as no other peaks are visible above this threshold. This hypothesis was proposed recently and is based on the fact that neutron diffraction mainly probes deuterium arrangement while metallic network is almost transparent to neutrons [41]. However, a second desorption event at 200 °C is noticeable on the desorption profile which might be attributed to the *fcc* to *bcc* phase transition, as proposed recently based on combined synchrotron radiation and neutron diffraction experiments during desorption from a high entropy material [41].

The TDS profiles of the hydrides with $x = 2$, 5 and 7 are shown in Figure 7a while the XRD of desorbed materials are displayed in Figure 7b. The desorption shifts to lower temperatures with increasing the Fe content (Figure 7a) which is in good agreement with the thermodynamic destabilization determined above. The onset temperature of desorption decreases from 155 to 130 °C with increasing Fe content. The XRD patterns of materials after TDS analysis (Figure 7b) demonstrate the recovery of the initial *bcc* lattice with very similar lattice parameters (3.126(1), 3.121(1) and 3.121(1) Å for $x = 2$, 5 and 7, respectively) to the initial ones (Table 1). Moreover, the alloy with $x = 7$ contains a main *bcc* phase along with 5% of C14 Laves intermetallic, in agreement with the initial structural analysis.

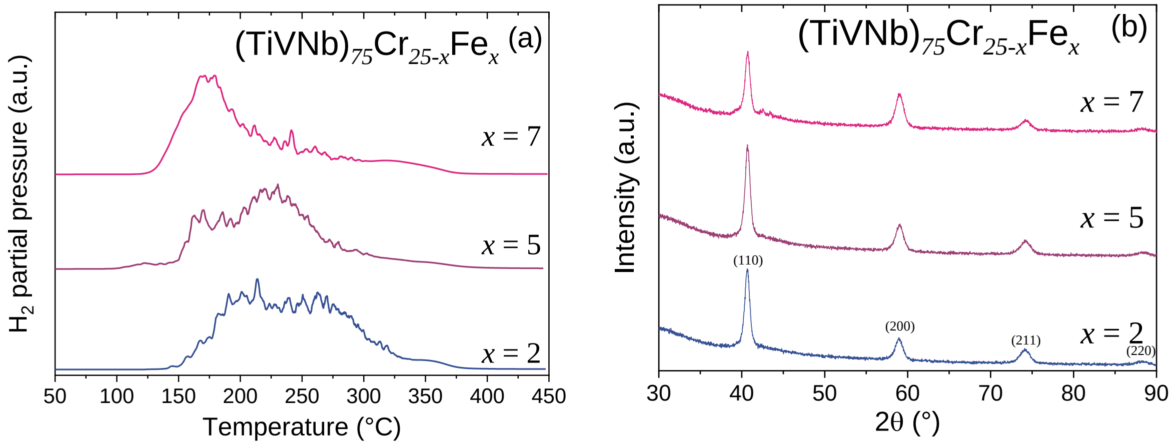

Figure 7. (a) TDS curves for the $(TiVNb)_{75}Cr_{25-x}Fe_x$ hydrides with $x = 2$, 5 and 7 recorded with 5 °C/min; (b) XRD patterns of the materials obtained after desorption.

The *in situ* neutron diffraction and TDS experiments conclude that the hydrogen absorption and desorption reactions into these alloys are fully reversible. All alloys absorb hydrogen forming a *fcc* hydride and desorb hydrogen to recover the initial *bcc* phase. Consequently, we tested the cycle-life stability of these three alloys, and the variation of the reversible capacity during cycling is plotted in Figure 8a, while the kinetic curves during absorption are shown in Figure 8b. A comparison of SR-XRD patterns ($\lambda = 0.1265$ Å) of as-synthesized and desorbed after cycling materials is displayed in Figure 8c (SI3-5 for details). Despite an obvious loss of capacity, the hydrogen absorption and desorption reactions are fully reversible and the overall capacity slightly decreases during cycling (~6-8 % after 15 cycles), in contrast to the pristine TiVCrNb alloy whose reversible capacity stabilizes after first 5 cycles [14]. The absorption kinetics are improved during the cycling due to the decrepitation effect. Overall, the three alloys quickly absorb hydrogen at room temperature reaching full capacity within the first minute, while the absorption rate slightly decreases with increasing Fe content (Figure 8b). From the structural point of view, the initial *bcc* lattice is maintained (Figure 8c) without any phase segregation or increase in the quantity of the C14 Laves intermetallic for the alloy initially containing this phase ($x = 7$). The *bcc* lattice parameters after cycling are slightly larger than the initial values and the diffraction peaks are broadened after cycling, irrespective of composition. These observations hint at two phenomena that might explain the progressive loss of capacity during cycling: a trapping of hydrogen or incomplete desorption under the present conditions and a development of defects during cycling, as already demonstrated for the TiVNbCr alloy [14]. The microstructure of the alloy with $x = 5$ is unchanged after cycling, as demonstrated by SEM-EDS (Figure SI3-6). Despite the gradual loss of capacity, the reversibility between the *fcc* hydride and the initial *bcc* lattice is maintained, without phase segregation or major microstructural changes, regardless of the composition.

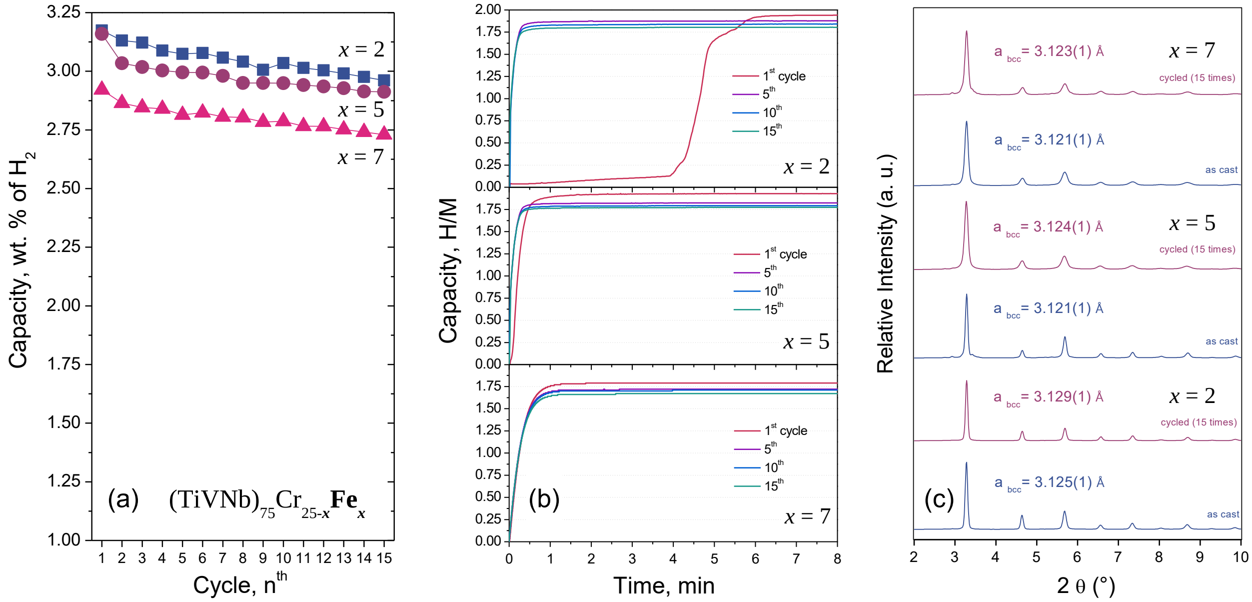

Figure 8. (a) Hydrogen absorption capacity during 15 absorption/desorption cycles for the $(TiVNb)_{75}Cr_{25-x}Fe_x$ ($x = 2$, 5 and 7) alloys; (b) absorption kinetic curves for the 1st, 5th, 10th and 15th cycles recorded under 35 bar and 25 °C, (c) SR-XRD ($\lambda = 0.1265$ Å) of powder samples as-synthesized and desorbed after 15 cycles.

Conclusions

This work demonstrates how ML predictions, corroborated by DFT calculations, can efficiently and expeditiously direct materials discovery efforts for hydrogen storage applications.

We specifically focused on the addition of Fe as low-cost raw material in a high-capacity HEA, TiVCrNb. This addition was predicted to thermodynamically destabilize the hydride phase with increasing x in the $(TiVNb)_{75}Cr_{25-x}Fe_x$ series (at the cost of reducing the storage capacity). To validate these predictions and assess its suitability for hydrogen storage, a detailed characterization of $(TiVNb)_{75}Cr_{25-x}Fe_x$ alloys with x = 2-15 has been carried out. This study elucidated Fe substitution effects on the structure, microstructure, and hydrogen sorption properties. While single-phase solid solutions with a *bcc* lattice can be obtained for a maximum of 5 at. % Fe, exceeding this limit leads to the progressive formation of a secondary C14 Laves phase with increasing x. The local structure of alloys up to $x = 7$ is well described as a random distribution of atoms within the *bcc* lattice without distortion. Hydrogen absorption experiments on *bcc* alloys with relatively small Fe substitution (x = 2, 5 and 7) most importantly confirm that substantial destabilization (up to ~10 kJ $molH_2^{-1}$ change in reaction enthalpy) of the *fcc* dihydride phase formation can be achieved, as predicted by ML and DFT approaches, albeit with a ~10% reduction in saturation capacity.

Notably, the hydrogen absorption and desorption reactions are fully reversible with good cycle-life performance, indicating that the Fe-substitution approach in refractory HEAs is a promising route to optimize hydrogen storage performances and lower the cost of these materials. Further research efforts should focus on several areas to improve fundamental understanding and optimize these HEA hydrides. For example, what co-substitutions can further destabilize the intermediate monohydride to the same thermodynamic stability of the *fcc* dihydride phase, and can such co-substitutions increase the Fe solubility in the *bcc* alloy phase without sacrificing further capacity? If such materials can be targeted and discovered that both have reversible capacity equal to the total capacity under mild desorption conditions and improve raw material costs (e.g., synthesis routes from ferrovanadium or ferroniobium), these materials may represent attractive alloys with double the capacity of traditional alloys (e.g. TiFe) for practical hydrogen storage applications.

Funding

AA, NPR and CZ acknowledge the funding from the French ANR MASSHY project ANR-19-CE05-0029-01. Work at the University of Nottingham is supported by EPSRC (EP/V042556/1) and Leverhulme Trust (Grant No. LIP-2021-018). The authors acknowledge the use of the ARCHER2 supercomputer through membership of the UK's HPC Materials Chemistry Consortium, which is funded by EPSRC (EP/X035859/1). MW, MA and VS gratefully acknowledge research support from the U.S. Department of Energy (DOE), Office of Energy Efficiency and Renewable Energy, Fuel Cell Technologies Office, through the Hydrogen Storage Materials Advanced Research Consortium (HyMARC). Their work was supported by the Laboratory Directed Research and Development (LDRD) program at Sandia National Laboratories.

Sandia National Laboratories is a multimission laboratory managed and operated by National Technology & Engineering Solutions of Sandia, LLC, a wholly owned subsidiary of Honeywell International Inc., for the U.S. Department of Energy's National Nuclear Security Administration (DOE/NNSA) under Contract DE- NA0003525. This written work is co-authored by an employee(s) of NTESS. The employee(s), not NTESS, owns the right, title, and interest in and to the written work and is responsible for its contents. Any subjective views or opinions that might be expressed in the written work do not necessarily represent the views of the U.S. Government. The publisher acknowledges that the U.S. Government retains a non-exclusive, paid-up, irrevocable, worldwide license to publish or reproduce the published form of this written work or allow others

to do so, for U.S. Government purposes. The DOE will provide public access to results of federally sponsored research in accordance with the DOE Public Access Plan.

Acknowledgements

Fabrice Couturas, Valérie Lalanne, Olivier Rouleau and Rémy Pires Brazuna from ICMPE (Institut de Chimie et des Matériaux Paris-Est, UMR 7182 CNRS-UPEC, Thiais, France) are acknowledged for their help with hydrogenation, arc-melting, XRD, SEM-EDX experiments, respectively. Jean-Marc Joubert from ICMPE is acknowledged for CALPHAD modeling with Thermo-Calc package. AA, NPR and CZ thank Faye Greaves from ICMPE and Sofien Djellit from D1B-ILL (Institut Laue-Langevin, Grenoble, France) for their help with neutron diffraction experiments at ILL.

References:

[1] M.D. Allendorf, V. Stavila, J.L. Snider, M. Witman, M.E. Bowden, K. Brooks, B.L. Tran, T. Autrey, Challenges to developing materials for the transport and storage of hydrogen, Nat. Chem. 14 (2022) 1214–1223. https://doi.org/10.1038/s41557-022-01056-2.

[2] U. Eberle, M. Felderhoff, F. Schuth, Chemical and Physical Solutions for Hydrogen Storage, Angew. Chem.-Int. Edit. 48 (2009) 6608–6630.

[3] M. Hirscher, V.A. Yartys, M. Baricco, J. Bellosta von Colbe, D. Blanchard, R.C. Bowman, D.P. Broom, C.E. Buckley, F. Chang, P. Chen, Y.W. Cho, J.-C. Crivello, F. Cuevas, W.I.F. David, P.E. de Jongh, R.V. Denys, M. Dornheim, M. Felderhoff, Y. Filinchuk, G.E. Froudakis, D.M. Grant, E.MacA. Gray, B.C. Hauback, T. He, T.D. Humphries, T.R. Jensen, S. Kim, Y. Kojima, M. Latroche, H.-W. Li, M.V. Lototskyy, J.W. Makepeace, K.T. Møller, L. Naheed, P. Ngene, D. Noréus, M.M. Nygård, S. Orimo, M. Paskevicius, L. Pasquini, D.B. Ravnsbæk, M. Veronica Sofianos, T.J. Udovic, T. Vegge, G.S. Walker, C.J. Webb, C. Weidenthaler, C. Zlotea, Materials for hydrogen-based energy storage – past, recent progress and future outlook, Journal of Alloys and Compounds 827 (2020) 153548. https://doi.org/10.1016/j.jallcom.2019.153548.

[4] F. Marques, M. Balcerzak, F. Winkelmann, G. Zepon, M. Felderhoff, Review and outlook on high-entropy alloys for hydrogen storage, Energy Environ. Sci. 14 (2021) 5191–5227. https://doi.org/10.1039/D1EE01543E.

[5] T.R. Somo, M.V. Lototskyy, V.A. Yartys, M.W. Davids, S.N. Nyamsi, Hydrogen storage behaviours of high entropy alloys: A Review, Journal of Energy Storage 73 (2023) 108969. https://doi.org/10.1016/j.est.2023.108969.

[6] M.M. Nygård, G. Ek, D. Karlsson, M. Sahlberg, M.H. Sørby, B.C. Hauback, Hydrogen storage in high-entropy alloys with varying degree of local lattice strain, International Journal of Hydrogen Energy (2019). https://doi.org/10.1016/j.ijhydene.2019.03.223.

[7] M.M. Nygård, G. Ek, D. Karlsson, M.H. Sørby, M. Sahlberg, B.C. Hauback, Counting electrons - A new approach to tailor the hydrogen sorption properties of high-entropy alloys, Acta Materialia 175 (2019) 121–129. https://doi.org/10.1016/j.actamat.2019.06.002.

[8] E. Halpren, X. Yao, Z.W. Chen, C.V. Singh, Machine learning assisted design of BCC high entropy alloys for room temperature hydrogen storage, Acta Materialia 270 (2024) 119841. https://doi.org/10.1016/j.actamat.2024.119841.

[9] M. Witman, S. Ling, D.M. Grant, G.S. Walker, S. Agarwal, V. Stavila, M.D. Allendorf, Extracting an Empirical Intermetallic Hydride Design Principle from Limited Data via Interpretable Machine Learning, J. Phys. Chem. Lett. 11 (2020) 40–47. https://doi.org/10.1021/acs.jpclett.9b02971.

[10] M. Witman, G. Ek, S. Ling, J. Chames, S. Agarwal, J. Wong, M.D. Allendorf, M. Sahlberg, V. Stavila, Data-Driven Discovery and Synthesis of High Entropy Alloy Hydrides with Targeted Thermodynamic Stability, Chem. Mater. 33 (2021) 4067–4076. https://doi.org/10.1021/acs.chemmater.1c00647.

[11] M.M. Nygård, W.A. Sławiński, G. Ek, M.H. Sørby, M. Sahlberg, D.A. Keen, B.C. Hauback, Local order in high-entropy alloys and associated deuterides – a total scattering and Reverse Monte Carlo study, Acta Materialia (2020). https://doi.org/10.1016/j.actamat.2020.08.045.

[12] N. Pineda-Romero, M. Witman, V. Stavila, C. Zlotea, The effect of 10 at.% Al addition on the hydrogen storage properties of the Ti0.33V0.33Nb0.33 multi-principal element alloy, Intermetallics 146 (2022) 107590. https://doi.org/10.1016/j.intermet.2022.107590.

[13] R.B. Strozi, B.H. Silva, D.R. Leiva, C. Zlotea, W.J. Botta, G. Zepon, Tuning the hydrogen storage properties of Ti-V-Nb-Cr alloys by controlling the Cr/(TiVNb) ratio, Journal of Alloys and Compounds 932 (2023) 167609. https://doi.org/10.1016/j.jallcom.2022.167609.

[14] R.B. Strozi, M. Witman, V. Stavila, J. Cizek, K. Sakaki, H. Kim, O. Melikhova, L. Perrière, A. Machida, Y. Nakahira, G. Zepon, W.J. Botta, C. Zlotea, Elucidating Primary Degradation Mechanisms in High-Cycling-Capacity, Compositionally Tunable High-Entropy Hydrides, ACS Appl. Mater. Interfaces 15 (2023) 38412–38422. https://doi.org/10.1021/acsami.3c05206.

[15] N. Pineda-Romero, C. Zlotea, Uncovering the Effect of Al Addition on the Hydrogen Storage Properties of the Ternary TiVNb Alloy, Materials 15 (2022) 7974. https://doi.org/10.3390/ma15227974.

[16] M.D. Witman, S. Ling, M. Wadge, A. Bouzidi, N. Pineda-Romero, R. Clulow, G. Ek, J.M. Chames, E.J. Allendorf, S. Agarwal, M.D. Allendorf, G.S. Walker, D.M. Grant, M. Sahlberg, C. Zlotea, V. Stavila, Towards Pareto optimal high entropy hydrides via data-driven materials discovery, J. Mater. Chem. A 11 (2023) 15878–15888. https://doi.org/10.1039/D3TA02323K.

[17] Y. Zhu, X.-S. Yang, Z.-L. Xu, G.C.-P. Tsui, Q. Zhou, R. Tang, F. Xiao, K. Chan, Development of AB2-type TiZrCrMnFeCoV intermetallic high-entropy alloy for reversible room-temperature hydrogen storage, Journal of Energy Storage 75 (2024) 109553. https://doi.org/10.1016/j.est.2023.109553.

[18] G.B.M. Vaughan, R. Baker, R. Barret, J. Bonnefoy, T. Buslaps, S. Checchia, D. Duran, F. Fihman, P. Got, J. Kieffer, S.A.J. Kimber, K. Martel, C. Morawe, D. Mottin, E. Papillon, S. Petitdemange, A. Vamvakeros, J.-P. Vieux, M. Di Michiel, ID15A at the ESRF – a beamline for high speed ıt operando X-ray diffraction, diffraction tomography and total scattering, Journal of Synchrotron Radiation 27 (2020) 515–528. https://doi.org/10.1107/S1600577519016813.

[19] G. Ashiotis, A. Deschildre, Z. Nawaz, J.P. Wright, D. Karkoulis, F.E. Picca, J. Kieffer, The fast azimuthal integration Python library: pyFAI, J Appl Cryst 48 (2015) 510–519. https://doi.org/10.1107/S1600576715004306.

[20] P. Juhás, T. Davis, C.L. Farrow, S.J.L. Billinge, PDFgetX3: a rapid and highly automatable program for processing powder diffraction data into total scattering pair distribution functions, J Appl Cryst 46 (2013) 560–566. https://doi.org/10.1107/S0021889813005190.

[21] C.L. Farrow, P. Juhas, J.W. Liu, D. Bryndin, E.S. Božin, J. Bloch, T. Proffen, S.J.L. Billinge, PDFfit2 and PDFgui: computer programs for studying nanostructure in crystals, J. Phys.: Condens. Matter 19 (2007) 335219. https://doi.org/10.1088/0953-8984/19/33/335219.

[22] J. Rodríguez-Carvajal, Recent advances in magnetic structure determination by neutron powder diffraction, Physica B: Condensed Matter 192 (1993) 55–69. https://doi.org/10.1016/0921-4526(93)90108-I.

[23] A. Le Bail, H. Duroy, J.L. Fourquet, Ab-initio structure determination of LiSbWO6 by X-ray powder diffraction, Materials Research Bulletin 23 (1988) 447–452. https://doi.org/10.1016/0025-5408(88)90019-0.

[24] C. Zlotea, C. Chevalier-César, E. Léonel, E. Leroy, F. Cuevas, P. Dibandjo, C. Vix-Guterl, T. Martens, M. Latroche, Synthesis of small metallic Mg-based nanoparticles confined in porous carbon materials for hydrogen sorption, Faraday Discussion 151 (2011) 117–131.

[25] M. Witman, M. Allendorf, V. Stavila, Database for machine learning of hydrogen storage materials properties, (2024). https://doi.org/10.5281/zenodo.10680097.

[26] M.M. Nygård, Ø.S. Fjellvåg, M.H. Sørby, K. Sakaki, K. Ikeda, J. Armstrong, P. Vajeeston, W.A. Sławiński, H. Kim, A. Machida, Y. Nakamura, B.C. Hauback, The average and local structure of TiVCrNbDx (x=0,2.2,8) from total scattering and neutron spectroscopy, Acta Materialia 205 (2021) 116496. https://doi.org/10.1016/j.actamat.2020.116496.

[27] T. Ferreira, N. Pineda-Romero, W.J. Botta, G. Zepon, C. Zlotea, Tuning the hydride stability of the TiVNb-based alloys by equimolar Cr/Al addition, Intermetallics 161 (2023) 107992. https://doi.org/10.1016/j.intermet.2023.107992.

[28] L. Ward, A. Agrawal, A. Choudhary, C. Wolverton, A general-purpose machine learning framework for predicting properties of inorganic materials, Npj Comput Mater 2 (2016) 1–7. https://doi.org/10.1038/npjcompumats.2016.28.

[29] S.M. Lundberg, S.-I. Lee, A unified approach to interpreting model predictions, in: Proceedings of the 31st International Conference on Neural Information Processing Systems, Curran Associates Inc., Red Hook, NY, USA, 2017: pp. 4768–4777.

[30] M.D. Witman, N.C. Bartelt, S. Ling, P.-W. Guan, L. Way, M.D. Allendorf, V. Stavila, Phase Diagrams of Alloys and Their Hydrides via On-Lattice Graph Neural Networks and Limited Training Data, J. Phys. Chem. Lett. 15 (2024) 1500–1506. https://doi.org/10.1021/acs.jpclett.3c03369.

[31] A.C. Switendick, Band Structure Calculations for Metal Hydrogen Systems*, Zeitschrift Für Physikalische Chemie 117 (1979) 89–112. https://doi.org/10.1524/zpch.1979.117.117.089.

[32] A. Borgschulte, J. Terreni, E. Billeter, L. Daemen, Y. Cheng, A. Pandey, Z. Łodziana, R.J. Hemley, A.J. Ramirez-Cuesta, Inelastic neutron scattering evidence for anomalous H–H distances in metal hydrides, PNAS 117 (2020) 4021–4026. https://doi.org/10.1073/pnas.1912900117.

[33] A. Andreasen, Predicting formation enthalpies of metal hydrides, Risø National Laboratory. Denmark. Forskningscenter Risoe. Risoe-R No. 1484(EN) (2004).

[34] D.B. Miracle, O.N. Senkov, A critical review of high entropy alloys and related concepts, Acta Materialia 122 (2017) 448–511. https://doi.org/10.1016/j.actamat.2016.08.081.

[35] M.M. Nygård, W.A. Sławiński, G. Ek, M.H. Sørby, M. Sahlberg, D.A. Keen, B.C. Hauback, Local order in high-entropy alloys and associated deuterides – a total scattering and Reverse Monte Carlo study, Acta Materialia 199 (2020) 504–513. https://doi.org/10.1016/j.actamat.2020.08.045.

[36] P. Edalati, R. Floriano, A. Mohammadi, Y. Li, G. Zepon, H.-W. Li, K. Edalati, Reversible room temperature hydrogen storage in high-entropy alloy TiZrCrMnFeNi, Scripta Materialia 178 (2020) 387–390. https://doi.org/10.1016/j.scriptamat.2019.12.009.

[37] A. Kumar, T.P. Yadav, N.K. Mukhopadhyay, Notable hydrogen storage in Ti–Zr–V–Cr–Ni high entropy alloy, International Journal of Hydrogen Energy 47 (2022) 22893–22900. https://doi.org/10.1016/j.ijhydene.2022.05.107.

[38] N. Pineda Romero, M. Witman, K. Harvey, V. Stavila, V. Nassif, E. Elkaïm, C. Zlotea, Large Destabilization of (TiVNb)-Based Hydrides via (Al, Mo) Addition: Insights from Experiments and Data-Driven Models, ACS Appl. Energy Mater. (2023). https://doi.org/10.1021/acsaem.3c02696.

[39] J.F. Lynch, J.J. Reilly, F. Millot, The absorption of hydrogen by binary vanadium-chromium alloys, Journal of Physics and Chemistry of Solids 39 (1978) 883–890. https://doi.org/10.1016/0022-3697(78)90150-6.

[40] C. Zlotea, A. Bouzidi, J. Montero, G. Ek, M. Sahlberg, Compositional effects on the hydrogen storage properties in a series of refractory high entropy alloys, Frontiers in Energy Research 10 (2022). https://www.frontiersin.org/articles/10.3389/fenrg.2022.991447 (accessed September 28, 2022).

[41] A. Bouzidi, E. Elkaim, V. Nassif, C. Zlotea, Effect of Cr/Mn Addition in TiVNb on Hydrogen Sorption Properties: Thermodynamics and Phase Transition Study, Hydrogen 5 (2024) 123–136. https://doi.org/10.3390/hydrogen5010008.

[42] D. Karlsson, G. Ek, J. Cedervall, C. Zlotea, K.T. Møller, T.C. Hansen, J. Bednarčík, M. Paskevicius, M.H. Sørby, T.R. Jensen, U. Jansson, M. Sahlberg, Structure and Hydrogenation Properties of a HfNbTiVZr High-Entropy Alloy, Inorg. Chem. 57 (2018) 2103–2110. https://doi.org/10.1021/acs.inorgchem.7b03004.

[43] J. Montero, G. Ek, L. Laversenne, V. Nassif, G. Zepon, M. Sahlberg, C. Zlotea, Hydrogen storage properties of the refractory Ti–V–Zr–Nb–Ta multi-principal element alloy, Journal of Alloys and Compounds 835 (2020) 155376. https://doi.org/10.1016/j.jallcom.2020.155376.